SUPPLEMENTARY INFORMATION
for
Observation of a tripartite quantum phase for coexisting extended, localized, and critical states

Zhongshu Hu,[1] Yajing Guo,[1] Yu-Dong Wei,[1] Bing-Chen Yao,[1] Zhentian Qian,[2] Xin-Chi Zhou,[3] Bao-Zong Wang,[1] Jianing Yang,[1] Xuzong Chen,[4] Shengjie Jin,[1,*] and Xiong-Jun Liu[1,†]

[1]*International Center for Quantum Materials, School of Physics, Peking University, Beijing 100871, China*
[2]*Cavendish Laboratory, University of Cambridge, JJ Thomson Avenue, Cambridge CB3 0HE, United Kingdom*
[3]*Max Planck Institute for the Physics of Complex Systems, Nöthnitzer Str. 38, 01187 Dresden, Germany*
[4]*School of Electronics, Peking University, Beijing 100871, China*

(Dated: March 31, 2026)

S1. TRIPARTITE QUANTUM PHASE

A. Analytical analysis

In the following, we first perform a quantitative analysis based on the concept of incomemensurately distributed zeros (IDZs) [1–3], which provides a mechanism for the emergence of a tripartite quantum phase featuring the coexistence of extended, localized, and critical states. After that, we provide a renormalization group treatment [4, 5], which independently corroborates the existence of critical states at zero energy.

1. Mechanism for the tripartite phase

As outlined in the main text, the coexistence of extended, localized, and critical states in the present model can be understood by analyzing eigenstates residing in distinct energy regimes. For convenience,we freeze the s orbital by taking $J_s \to 0$ and consider parameters satisfying $J_p \geq \delta_s \sim \delta_p > \Omega$. In this regime, spectrum with energies $|E| \leq \delta_s$ displays emergent spectral singularities, leading to either localized or critical behavior depending on the eigen-energy, whereas eigenstates with $|E| > \delta_s$ are free of such singularities and remain extended, as we provide detailed analysis below.

To facilitate the discussion, we rewrite the Hamiltonian Eq. (8) in main text as

$$\hat{H} = \sum_j \left(\hat{c}^\dagger_{j+1}\Pi_j\hat{c}_j + \text{H.c.}\right) + \hat{c}^\dagger_j M_j \hat{c}_j, \tag{S1}$$

with $\hat{c}^\dagger_j = (a^\dagger_j, b^\dagger_j)$, and the hopping coupling matrix and on-site matrix are given by

$$\begin{aligned}
\Pi_j &= \begin{pmatrix} -J_s & 0 \\ 0 & J_p \end{pmatrix} = t_+\sigma_0 + t_-\sigma_z, \\
M_j &= \begin{pmatrix} \delta_s\cos(2\pi\alpha j) & \mathrm{i}\Omega\sin(2\pi\alpha j) \\ -\mathrm{i}\Omega\sin(2\pi\alpha j) & \delta_p\cos(2\pi\alpha j) \end{pmatrix} = \bar{\delta}\cos(2\pi\alpha j)\sigma_0 + \Omega\sin(2\pi\alpha j)\sigma_y + \delta'\cos(2\pi\alpha j)\sigma_z.
\end{aligned} \tag{S2}$$

Here $t_\pm = (-J_s \pm J_p)/2$, $\bar{\delta} = (\delta_s + \delta_p)/2$, $\delta' = (\delta_s - \delta_p)/2$, and $\sigma_{0,x,y,z}$ are the identity and Pauli matrices. For experimentally relevant parameters, $J_s \ll J_p$, allowing us to approximate $J_s \simeq 0$. Under this condition, the hopping coupling matrix satisfies $\det\Pi_j = 0$, allowing the model to be effectively reduced to a spinless form. For an eigenstate $H|\psi\rangle = E|\psi\rangle$, we denote the wavefunction as $|\psi\rangle = \sum_j (u_j\hat{b}^\dagger_j + v_j\hat{a}^\dagger_j)|0\rangle$, where u_j and v_j denote amplitudes on the p and s orbitals, respectively. The corresponding coupled equations read

$$\begin{aligned}
J_p u_{j+1} + J_p u_{j-1} + \delta_p\cos(2\pi\alpha j)u_j + \mathrm{i}\Omega\sin(2\pi\alpha j)v_j &= Eu_j, \\
\delta_s\cos(2\pi\alpha j)v_j - \mathrm{i}\Omega\sin(2\pi\alpha j)u_j &= Ev_j.
\end{aligned} \tag{S3}$$

* jinshengjie@pku.edu.cn

† xiongjunliu@pku.edu.cn

By algebraically eliminating v_j, corresponding physically to integrating out the frozen s orbital, one obtains an effective single-component recursion relation for u_j. The resulting equation reads

$$J_p\left(u_{j-1}+u_{j+1}\right)+\left[\delta_p\cos(2\pi\alpha j)+\frac{\Omega^2\sin^2(2\pi\alpha j)}{E-\delta_s\cos(2\pi\alpha j)}\right]u_j=Eu_j. \tag{S4}$$

The system is thus effectively mapped onto a spinless quasiperiodic model with uniform hopping amplitude J_p. The energy-dependent on-site potential encodes the influence of s-p inter-orbital coupling and is given by

$$V_{\mathrm{eff},j}=\delta_p\cos(2\pi\alpha j)+\frac{\Omega^2\sin^2(2\pi\alpha j)}{E-\delta_s\cos(2\pi\alpha j)}. \tag{S5}$$

This expression immediately reveals a qualitative distinction between energy regimes. For $|E|>\delta_s$, the denominator remains finite for all $\tilde{j}$, ensuring that $V_{\mathrm{eff},\tilde{j}}$ is bounded and smooth. In contrast, for $|E|<\delta_s$, there exist incommensurate sites j_0 satisfying $E-\delta_s\cos(2\pi\alpha j_0)=0$, at which $V_{\mathrm{eff},j}$ diverges.

The eigenstates close to the band edge, with $|E|>\delta_s$, are extended states. Since such energies lie outside the range of the s-orbital on-site energy, they are mainly contributed by the p-orbital component, where the hopping amplitude J_p dominates over the quasiperiodic modulation, thus resulting in extended states.

For the eigenstates within the s orbital onsite energy $|E|<\delta_s$, the eigenstates can be either localized or critical states, depending on the details of the state. The inter-orbital coupling in Eq. (S2) facilitates a complete transition from p to s orbitals at the $\tilde{j}$-sites where $\delta_{s,\tilde{j}}=E$, which are incommensurately distributed throughout the system. This full transition to the s-orbital hinders the tunneling of the p orbitals across those sites, resulting in incommensurately distributed zeros (IDZs) in hopping—a central mechanism leading to the emergence of critical states, as captured by Avila's profound global theory [1, 2].

With the presence of IDZs, two distinct scenarios follow. For states with $|E|\lesssim\delta_s$, eigenstates reside near extrema of the onsite potential $\delta_{i,j}$ and are significantly influenced by the quasiperiodic potential, resulting in localized states. In contrast, states with $E\sim 0$ are primarily located at the nodes of the onsite potential $\delta_{s,j}\sim\cos(2\pi\alpha j)$, where the inter-orbital coupling $\sim\sin(2\pi\alpha j)$ is relatively strong. These states are less affected by the quasiperiodic potential, resulting in delocalization. Consequently, the IDZs effectively partition the lattice into segments, within which the delocalized wavefunction reorganizes self-similarly, giving rise to scale-free critical states.

The appearance of critical states near $E\sim 0$ motivates a renormalization-group analysis of the coupling flow at zero energy, which we present in the following section.

2. *Renormalization group analysis*

The statement that the eigenstates near $E\sim 0$ are critical can be further corroborated through a renormalization group analysis based on iteration of commensurate approximation [4, 5]. The renormalization group (RG) framework analyzes the relevance of effective hopping coefficients by iteratively applying rational approximations to the quasiperiodic (QP) parameter. Concretely, one considers a sequence of rationals $\alpha^{(n)}=p_n/q_n$ that define a family of periodic Hamiltonians $H^{(n)}$, which recover the true quasiperiodic regime only in the irrational limit $\alpha=\alpha^{(\infty)}$. The RG flow as $n\to\infty$ then dictates the asymptotic properties of the eigenstates in the QP system. For each rational approximation, the spectrum of $H^{(n)}$ forms a periodic function of the quasi-momenta κ_x and κ_y. To systematically track how the renormalized coefficients evolve with system size, we evaluate the characteristic determinant

$$P^{(n)}=\left|\mathcal{H}^{(n)}-E\right| \tag{S6}$$

at a target energy E for a system size $L=F_n$, which can be expressed as

$$\begin{aligned}P^{(n)}(E;\kappa_x,\kappa_y)=\;&t_R^{(n)}\cos(\kappa_x+\kappa_x^0)+V_R^{(n)}\cos(\kappa_y+\kappa_y^0)\\&+C_R^{(n)}\cos(\kappa_x+\tilde{\kappa}_x^0)\cos(\kappa_y+\tilde{\kappa}_y^0)\\&+\epsilon_R^{(n)}(E,\varphi,\kappa)+T_R^{(n)}(E),\end{aligned} \tag{S7}$$

where $\epsilon_R^{(n)}$ contains higher-order harmonics that become irrelevant under the RG flow.

The long-scale nature of the eigenstates is governed by the relative scaling of the renormalized hopping amplitudes. For extended states, hopping along the x direction dominates, such that $|C_R^{(n)}/t_R^{(n)}|,|V_R^{(n)}/t_R^{(n)}|\to 0$. For localized states, hopping is primarily along y, giving $|t_R^{(n)}/V_R^{(n)}|,|C_R^{(n)}/V_R^{(n)}|\to 0$. Critical states emerge when all three hopping terms remain equally relevant, characterized by $|C_R^{(n)}/V_R^{(n)}|,|C_R^{(n)}/t_R^{(n)}|\gtrsim 1$. The RG flow thus provides a systematic means to identify transitions among extended, localized, and critical phases, as well as to locate mobility edges that appear as energy-dependent transition points.

To explicitly characterize the localized, critical, and extended regions in our incommensurate s-p orbital lattices, where we calculate the characteristic polynomial of commensurate approximates (CA) of the system at thermodynamic limit and compare different renormalized factors. The characteristic polynomial $P^{(L)}(E;\varphi,\kappa)=\det(H(\varphi,\kappa)-E)$ for any CA at system length L, boundary phase twist $\kappa=Lk$, accumulated initial phase $\varphi=L\phi$ and energy E is calculated as

$$P^{(L)}(E;\varphi,\kappa)=\det\begin{pmatrix} H_0-EI_2 & Te^{i\kappa} & 0 & \cdots & 0 & T^\dagger e^{-i\kappa} \\ T^\dagger e^{-i\kappa} & H_1-EI_2 & Te^{i\kappa} & \cdots & 0 & 0 \\ 0 & T^\dagger e^{-i\kappa} & H_2-EI_2 & \ddots & \vdots & \vdots \\ \vdots & \vdots & \ddots & \ddots & Te^{i\kappa} & 0 \\ 0 & 0 & \cdots & T^\dagger e^{-i\kappa} & H_{L-2}-EI_2 & Te^{i\kappa} \\ Te^{i\kappa} & 0 & \cdots & 0 & T^\dagger e^{-i\kappa} & H_{L-1}-EI_2 \end{pmatrix}, \tag{S8}$$

where

$$T=\begin{pmatrix}0 & 0\\ 0 & J_p\end{pmatrix},\quad H_j=\begin{pmatrix}\delta_s\cos(2\pi\alpha j+\phi) & i\Omega\sin(2\pi\alpha j+\phi)\\ -i\Omega\sin(2\pi\alpha j+\phi) & \delta_p\cos(2\pi\alpha j+\phi)\end{pmatrix},\ j=0,1,\ldots,L-1, \tag{S9}$$

and I_2 is the 2×2 identity matrix. This is a periodic function of κ and φ. By expanding $P^{(L)}(E;\varphi,\kappa)$ on different frequencies of κ and φ, the factors before $e^{i\kappa}, e^{i\varphi}$ and $e^{i(\kappa+\varphi)}$, denoted as $t_R^{(L)}(E), V_R^{(L)}(E)$ and $C_R^{(L)}(E)$ respectively, determines whether a state is in localized, extended or critical phase. We analyze these factors by carefully counting the phase factors. To accumulate a k-dependence of e^{iLk}, the only choice is to multiple L off-diagonal block J_p terms together, thus the factors $C_R^{(L)}(E)$ and $t_R^{(L)}(E)$ are completely contributed from

$$J_p^L\Pi_{j=0}^{L-1}\left[\delta_s\cos(2\pi j\alpha+\phi)-E\right] \tag{S10}$$

For a general J_p, the determination of $V_R^{(L)}(E)$ is complicated since after picking $Le^{i\phi}$ terms, the leftover L terms are picked among $e^{i\phi}$ terms, e^{ik} terms or constant phase dependency terms in various ways. However, for small J_p compared to other parameters, the contribution from off-diagonal blocked can be safely ignored, leaving the coefficient determinable by multiplication of determinants of diagonal 2×2 blocks,

$$\Pi_{j=0}^{L-1}\left[\left(\delta_s\delta_p+\Omega^2\right)\cos^2(2\pi j\alpha+\phi)-E\left(\delta_s+\delta_p\right)\cos(2\pi j\alpha+\phi)+\left(E^2-\Omega^2\right)\right] \tag{S11}$$

By evaluating these two expressions, we derive the desired renormalized factors. Calculation of all these factors thus break down to multiplications of the form $b\cos(2\pi j\alpha+\phi)+a$, which we calculate exactly with the following lemma.

Lemma S1.1. *For $\alpha=\frac{p}{L}$ with p coprime to L, we have*

$$\prod_{j=0}^{L-1}\left[b\cos(2\pi j\alpha+\phi)+a\right]=\left(-\tfrac{1}{2}\right)^{L-1}b^L\Big[\cos(L\phi)-(-1)^LT_L\left(\tfrac{a}{b}\right)\Big], \tag{S12}$$

where T_L is the L-th Chebyshev polynomial.

Proof. Take $z_j=e^{i(2\pi j\alpha+\phi)}$ and $c=\frac{2a}{b}$. The left-hand side can be rewritten as

$$\prod_{j=0}^{L-1}\left[b\cos(2\pi j\alpha+\phi)+a\right]=\left(\frac{b}{2}\right)^L\prod_{j=0}^{L-1}\left(z_j+z_j^{-1}+\frac{2a}{b}\right)=\left(\frac{b}{2}\right)^L\prod_{j=0}^{L-1}z_j^{-1}\prod_{j=0}^{L-1}\left(z_j^2+cz_j+1\right).$$

The first product can be evaluated straightforwardly as $\prod_{j=0}^{L-1}z_j^{-1}=e^{-iL\phi}\,e^{-i\pi\alpha L(L-1)}$. For the second product, each quadratic factor can be decomposed as $z_j^2+cz_j+1=(z_j-r_+)(z_j-r_-)$, where $r_\pm=\frac{-c\pm\sqrt{c^2-4}}{2}$ are the two roots of the characteristic equation. To proceed, we introduce the L-th root of unity $\omega = e^{i2\pi\alpha}$, such that $z_j = e^{i\phi}\omega^j$. Thus

$$\begin{aligned}
\prod_{j=0}^{L-1}[b\cos(2\pi j\alpha+\phi)+a] &= \left(\frac{b}{2}\right)^L e^{iL\phi}\,\omega^{-\frac{L(L-1)}{2}}\prod_{j=0}^{L-1}\left(-\omega^j+r_+e^{-i\phi}\right)\prod_{j=0}^{L-1}\left(-\omega^j+r_-e^{-i\phi}\right)\\
&= \left(\frac{b}{2}\right)^L e^{iL\phi}\,\omega^{-\frac{L(L-1)}{2}}\left(r_+^L e^{-iL\phi}-1\right)\left(r_-^L e^{-iL\phi}-1\right)\\
&= \left(\frac{b}{2}\right)^L (-1)^{p(L-1)}e^{iL\phi}\left[r_+^L r_-^L e^{-2iL\phi}+1-(r_+^L+r_-^L)e^{-iL\phi}\right]\\
&= \left(-\tfrac{1}{2}\right)^{L-1} b^L\left(\frac{e^{iL\phi}+e^{-iL\phi}}{2}-\frac{r_+^L+r_-^L}{2}\right)\\
&= \left(-\tfrac{1}{2}\right)^{L-1} b^L\Big[\cos(L\phi)-(-1)^L T_L\left(\tfrac{a}{b}\right)\Big].
\end{aligned} \tag{S13}$$

This proves the lemma. □

Using the lemma, the RG coefficients at $L\to\infty$ are obtained as

$$t_R^{(L)}(E) \sim \left(\tfrac{J_p\delta_s}{2}\right)^L T_L\left(\tfrac{E}{\delta_s}\right) \sim \begin{cases} \left(\frac{J_p\delta_s}{2}\right)^L, & |E|<|\delta_s|,\\ \left[\frac{J_p\left(|E|+\sqrt{E^2-\delta_s^2}\right)}{2}\right]^L, & |E|>|\delta_s|,\end{cases}$$

$$\begin{aligned}
V_R^{(L)}(E) &\gtrsim \left(\tfrac{\delta_s\delta_p+\Omega^2}{4}\right)^L\Bigg[T_L\left(\frac{E(\delta_s+\delta_p)+\sqrt{E^2(\delta_s+\delta_p)^2-4(E^2-\Omega^2)(\delta_s\delta_p+\Omega^2)}}{2(\delta_s\delta_p+\Omega^2)}\right)\\
&\qquad + T_L\left(\frac{E(\delta_s+\delta_p)-\sqrt{E^2(\delta_s+\delta_p)^2-4(E^2-\Omega^2)(\delta_s\delta_p+\Omega^2)}}{2(\delta_s\delta_p+\Omega^2)}\right)\Bigg]\\
&\sim \left(\tfrac{\delta_s\delta_p+\Omega^2}{4}\right)^L\max\{w_\pm^L, w_\pm^{-L}\},
\end{aligned} \tag{S14}$$

where

$$w_\pm = \left|z_\pm+\sqrt{z_\pm^2-1}\right|, \qquad z_\pm = \frac{E(\delta_s+\delta_p)\pm\sqrt{E^2(\delta_s+\delta_p)^2-4(E^2-\Omega^2)(\delta_s\delta_p+\Omega^2)}}{2(\delta_s\delta_p+\Omega^2)}. \tag{S15}$$

Finally,

$$C_R^{(L)}(E) \sim \left(\tfrac{J_p\delta_s}{2}\right)^L. \tag{S16}$$

Where the approximate equality holds at small J_p for the second equation, $w_\pm = \left|z_\pm+\sqrt{z_\pm^2-1}\right|, z_\pm = \frac{E(\delta_s+\delta_p)\pm\sqrt{E^2(\delta_s+\delta_p)^2-4(E^2-\Omega^2)(\delta_s\delta_p+\Omega^2)}}{2(\delta_s\delta_p+\Omega^2)}$. Coefficients of order $o\left(e^L\right)$ have been ignored at thermodynamic limit. Note the second equation is also exact at $E=0$ regardless of the value of J_p, since if $E=0$, the leftover terms can be picked only among $e^{i\phi}$ terms and e^{ik} terms. Then take CAs with an odd L, for example take only odd terms in the Fibonacci sequence. Now $e^{i\phi}$ terms and e^{ik} terms must contribute a total of zero phase altogether while there is an odd number of phase factors to pick, giving a contradiction, leading to no $e^{i\varphi}$ terms. Instead we must consider $e^{2i\varphi}$ term, given as $V_{2R}^{(L)}(E)\sim\left(\frac{\delta_s\delta_p+\Omega^2}{4}\right)^L$, which is exactly $\lim_{E\to 0}V_R^{(L)}(E)$. Consequently, the phase structure and phase transitions of the model are determined by this limiting behavior. At $E=0$, one can rigorously compare the relative magnitudes of the three terms, yielding

$$\frac{C_R^{(L)}(E=0)}{t_R^{(L)}(E=0)} = 1, \qquad \frac{C_R^{(L)}(E=0)}{V_R^{(L)}(E=0)} \sim \left(\frac{2J_p\delta_s}{\delta_s\delta_p+\Omega^2}\right)^L. \tag{S17}$$

This result implies that critical states appear strictly at zero energy whenever the condition $\Omega^2+\delta_s\delta_p \le 2\delta_s J_p$ is satisfied, which holds under the experimental parameters considered here.

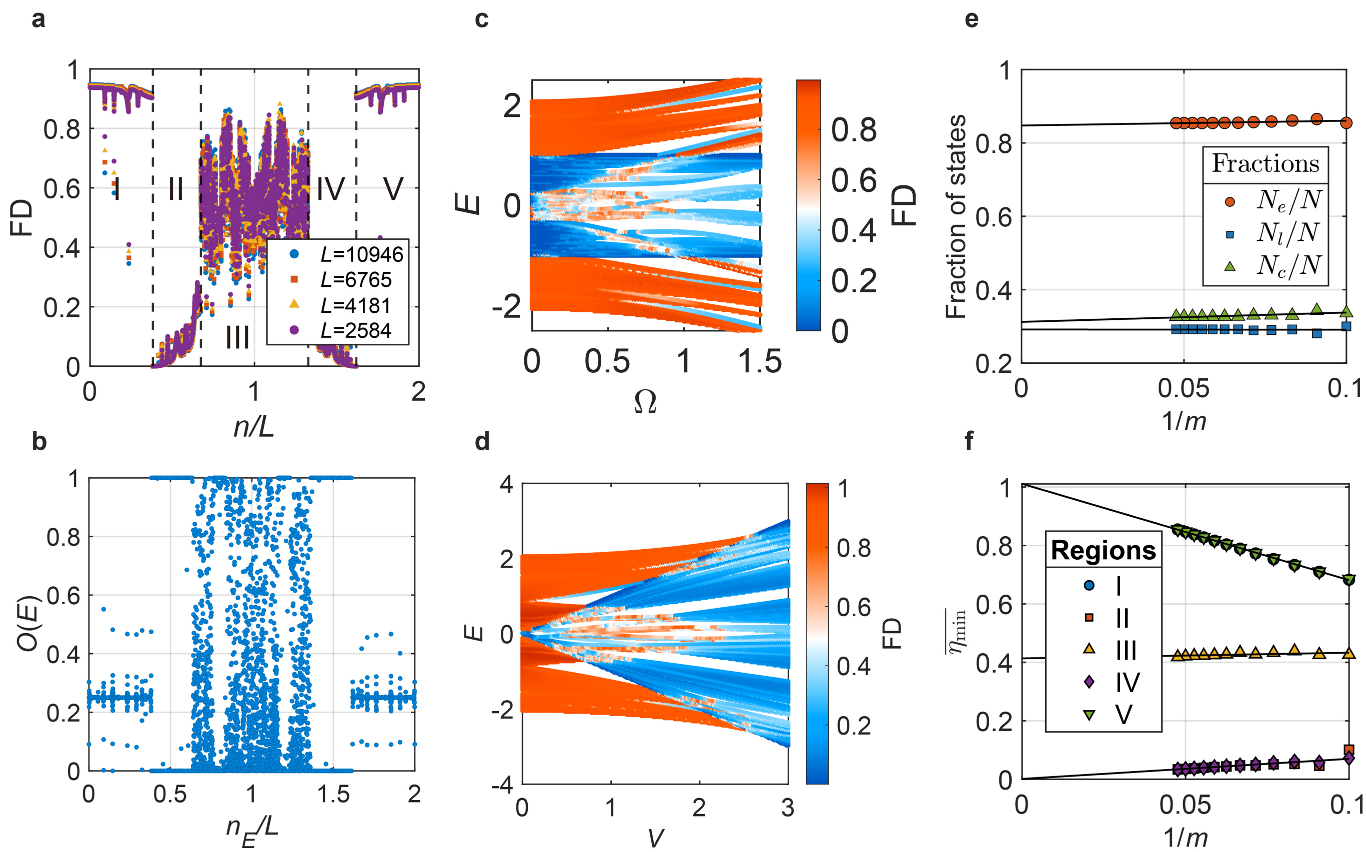

Figure S1. Numerical results of the orbital quasiperiodic lattice model. **a**, Fractal dimension (FD) versus state index n for different system sizes L, with parameters $V = J_p$, $\Omega = 0.5J_p$, $\Delta = 0$, $\alpha = (\sqrt{5}-1)/2$. Five distinct regions can be identified. **b**, Quarter-lattice occupation number $O(E)$[6] versus state index n_E for $L = 6765$, corresponding to the regions in (**a**). **c**,**d**, FD as a function of coupling Ω and quasiperiodic strength V. The light red region represents the critical regime. **e**,**f**, Finite-size scaling: the fractions of three types of states (**e**) and the scaling of $\overline{\eta_{\min}}$ (**f**) for various Fibonacci system sizes $L = F_m$.

B. Numerical results

To further validate the existence of the tripartite quantum phase, we perform comprehensive numerical simulations on the effective Hamiltonian $\hat{H}_{\text{eff}}$ defined in Eq. (8) (main text). Our investigation focuses on characterizing the localization properties of the entire energy spectrum through exact diagonalization (ED) and finite-size scaling analysis. By computing a suite of complementary diagnostics—including the fractal dimension (FD), the quarter-lattice occupation number $O(E)$, and the averaged minimal scaling exponent $\overline{\eta_{\min}}$—we provide a multi-dimensional perspective on the distinct transport and spatial properties of the localized, extended, and critical states.

Specifically, we first evaluate the FD for each eigenstate $|\psi_n\rangle$, defined as:

$$\text{FD} = -\frac{\ln\left(\sum_j |u_{j,n}|^4 + |v_{j,n}|^4\right)}{\ln L}, \tag{S18}$$

where $u_{j,n}$ and $v_{j,n}$ are the amplitudes of the n-th eigenstate on the s and p orbitals at site j, respectively. The FD serves as a sensitive probe for the spatial structure of the wave function: in the thermodynamic limit, FD $\to 1$ for delocalized (extended) states, FD $\to 0$ for localized states, while a fractional value $0 < \text{FD} < 1$ signifies the self-similar, multi-fractal nature characteristic of critical states. Additionally, we calculate the quarter-lattice occupation number $O(E) = \sum_{j=1}^{L/4}\langle\psi_E|\hat{n}_{j,s} + \hat{n}_{j,p}|\psi_E\rangle$ to assess the spatial distribution of the particle density across the lattice. For delocalized states, the density is expected to be uniformly distributed, yielding $O(E) \approx 1/4$, whereas localized states tend to cluster in specific regions, leading to $O(E)$ values near 0 or 1, depending on the localization center [6].

The numerical results presented in Fig. S1a,b reveal a clear tripartite separation within the energy spectrum. Based on the calculated FD and $O(E)$, we identify five distinct spectral regions. In regions I and V, the eigenstates exhibit FD ≈ 1 and $O(E) \approx 1/4$, which are the hallmark signatures of extended states. Conversely, regions II and IV are characterized by FD ≈ 0

and $O(E)$ values approaching the boundaries of 0 or 1, indicating strong localization. Most importantly, region III displays intermediate FD values and significant fluctuations in $O(E)$, providing robust evidence for the emergence of critical states. This tripartite structure is further explored in Fig. S1c,d, where we map the FD as a function of the interorbital coupling Ω and the quasiperiodic strength V. The resulting phase diagrams clearly delineate the boundaries of the critical regime, highlighting how the interplay between orbital hybridization and quasiperiodicity reshapes the localization landscape.

Finally, to ensure that these observations persist in the thermodynamic limit, we perform a rigorous finite-size scaling analysis. We select system sizes $L = F_m$ corresponding to the Fibonacci sequence to maintain the self-similarity of the quasiperiodic potential. As shown in Fig. S1e,f, we track the fraction of each type of state and the averaged minimal exponent $\overline{\eta_{\min}}$, defined as:

$$\overline{\eta_{\min}} = \frac{1}{N_s} \sum_{\text{states in region}} \eta_{\min}, \quad \text{with} \quad \eta_{\min} = \min_j \left\{ -\frac{\ln(n_{j,s} + n_{j,p})}{\ln L} \right\}. \tag{S19}$$

The scaling exponent $\eta_{\min}$ is a powerful tool for distinguishing localization properties: as $L \to \infty$, it converges to 1 for extended states, 0 for localized states, and a value between 0 and 1 for critical states. Our scaling results demonstrate that $\overline{\eta_{\min}}$ for each identified region converges toward these distinct asymptotic limits, confirming that the tripartite quantum phase is a robust feature of the system rather than a finite-size effect [2, 7, 8].

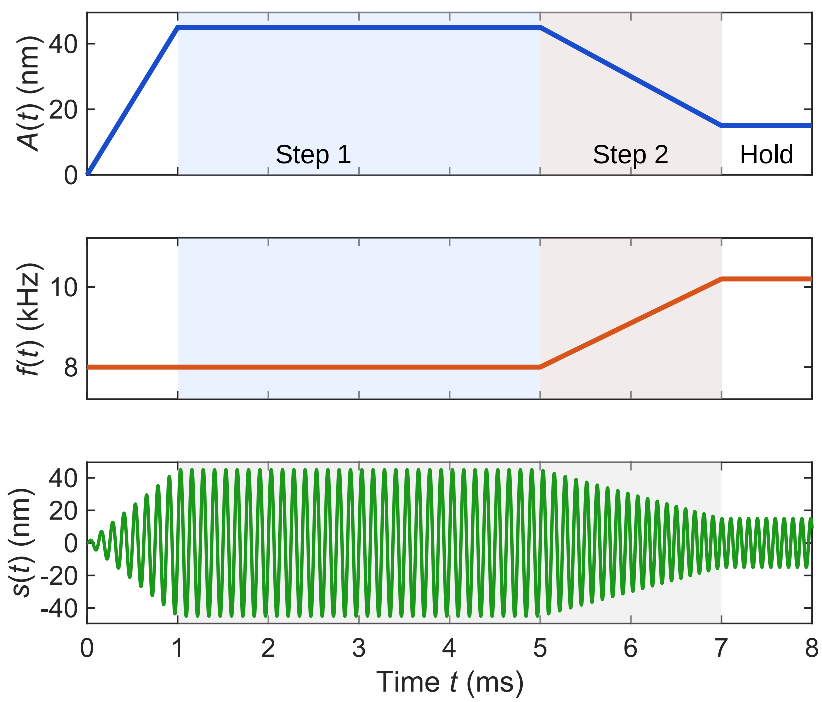

Figure S2. Timing sequence of lattice shaking. **a**–**c**, Time dependence of the shaking amplitude $A(t)$, frequency $f(t)$, and displacement $s(t)$. As an example, we show the case with initial shaking frequency $f_i = 8\,\mathrm{kHz}$ and amplitude $A_i = 45\,\mathrm{nm}$.

S2. CALIBRATION OF THE EFFECTIVE COUPLING STRENGTH

We experimentally find that at sufficiently large coupling strengths the atoms can be prepared in an excited extended state characterized by four momentum peaks, which we denote as the E_2 state. This state corresponds to an excited eigenstate of the effective Hamiltonian, as indicated in Fig. S4a. The E_2 state can be prepared either by ramping the shaking amplitude or shaking frequency. Taking ramping the shaking amplitude as an example, in practice we linearly ramp the shaking amplitude from 0 to A within $5\,\mathrm{ms}$ with shaking frequency fixed, and subsequently perform TOF measurements to obtain the momentum distribution, as indicated in the purple arrow in Fig. S3a. The measured momentum distributions as a function of the final amplitude A are shown in the lower row of Fig. S3. As A increases, the momentum distribution evolves from the initially localized state to a two-peak distribution. The observed asymmetry, with peaks appearing only on the left-hand side, arises from Floquet micromotion[9–13]: the peak positions alternate with the driving phase, and we choose the evolution time such that atoms predominantly condense on the left side. This behavior is consistent with the spectrum obtained from the effective

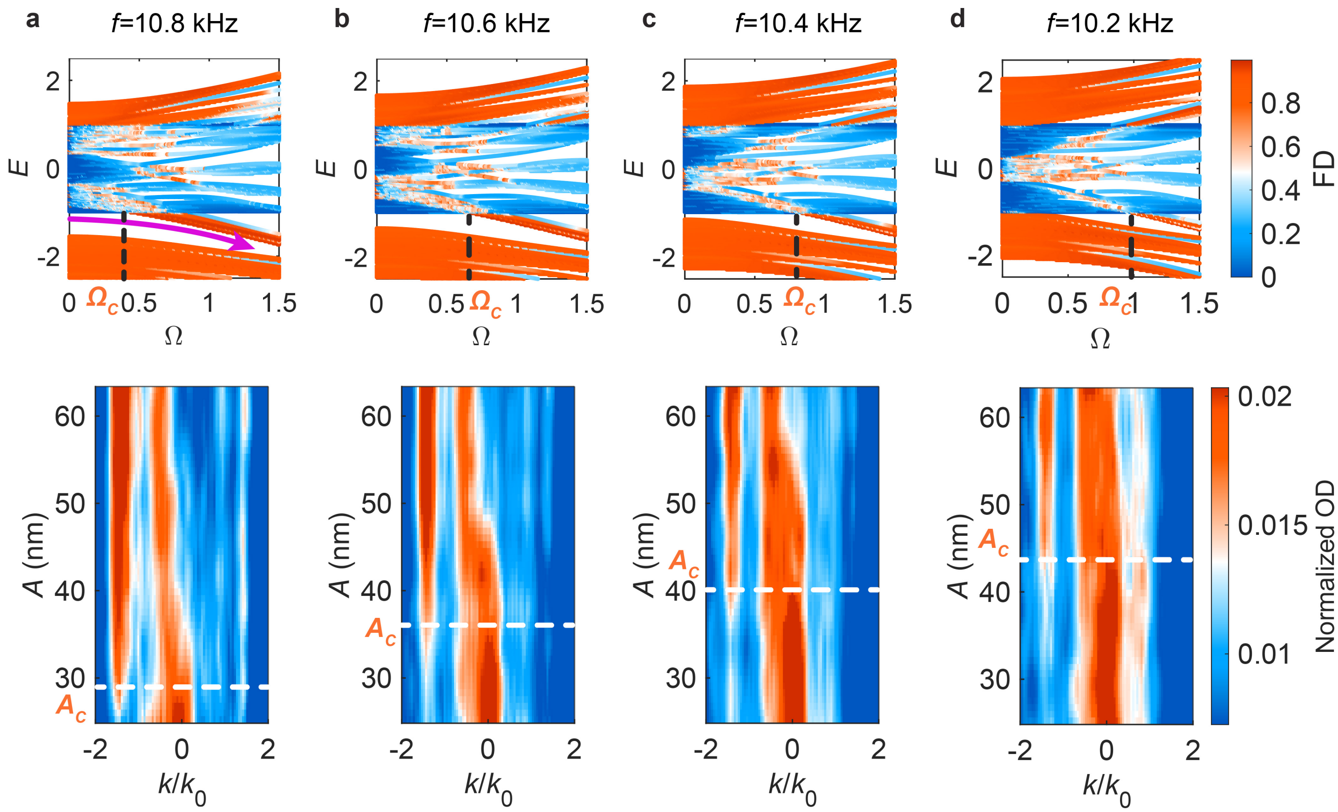

Figure S3. Calibration of the effective coupling strength. The shaking frequency is held fixed while the amplitude is linearly ramped from 0 to A within $5\,\mathrm{ms}$, followed by time-of-flight (TOF) measurement of the momentum distribution. As the final amplitude A increases, the momentum distribution changes from a localized state to a two-peak distribution. This process corresponds to a Landau–Zener transition in the spectrum, as indicated by the arrow in (**a**). When the coupling strength exceeds the critical value Ω_c, the state evolves into an extended state with four momentum peaks in the first two Brillouin zones. In the experiment, only two peaks are observed due to Floquet micromotion. Measurements performed at different shaking frequencies yield the critical amplitudes A_c, which quantitatively map the experimental shaking amplitude to the effective coupling strength Ω of the tight-binding model.

Hamiltonian calculation (upper row of Fig. S3), where the initial atoms evolve from the s-band ground state to an extended state with increasing coupling strength. Beyond a critical coupling Ω_c, the atoms transfer into this excited extended branch. Moreover, Ω_c depends on the shaking frequency f: as f decreases, Ω_c shifts to higher values, in agreement with experimental observations. Fig. S3a-d show the evolution at different shaking frequencies, demonstrating that the critical shaking amplitude A_c at which the transition occurs systematically increases with decreasing frequency. The model parameters are fixed as $V = J_p = 1$ and $\alpha = 1.411$, and all energies are expressed in units of J_p. Thus, we can build a bridge from our experimental parameters to the tight-binding parameters of the effective Hamiltonian.

S3. STATE PREPARATION

This section provides additional details on the state preparation procedure. The general preparation scheme and the underlying physical picture have been described in the main text. The shaking pulse sequence used in the two-stage protocol is presented in the Methods section and illustrated in Fig. S2. Here we focus on how different choices of the initial shaking parameters f_i and A_i lead to distinct final states, and provide representative TOF images characterizing each state.

Among the eigenstates of Hamiltonian Eq. (8) (main text), the fractal dimensions and momentum distributions of four representative states are shown in Fig. S4a. By dynamically ramping the Hamiltonian parameters, we are able to prepare all of these states. The extended ground state (E_1) is prepared by sweeping the shaking frequency from an initial f_i to the final frequency. When the coupling is sufficiently strong, the atoms are transferred adiabatically into the bottom of the p-band, corresponding to the E_1 state.

In contrast, preparation of the critical state requires a two-step process mediated by the excited extended state (E_2). As established in the calibration measurements, the E_2 state can be prepared either by ramping the shaking amplitude or by ramping

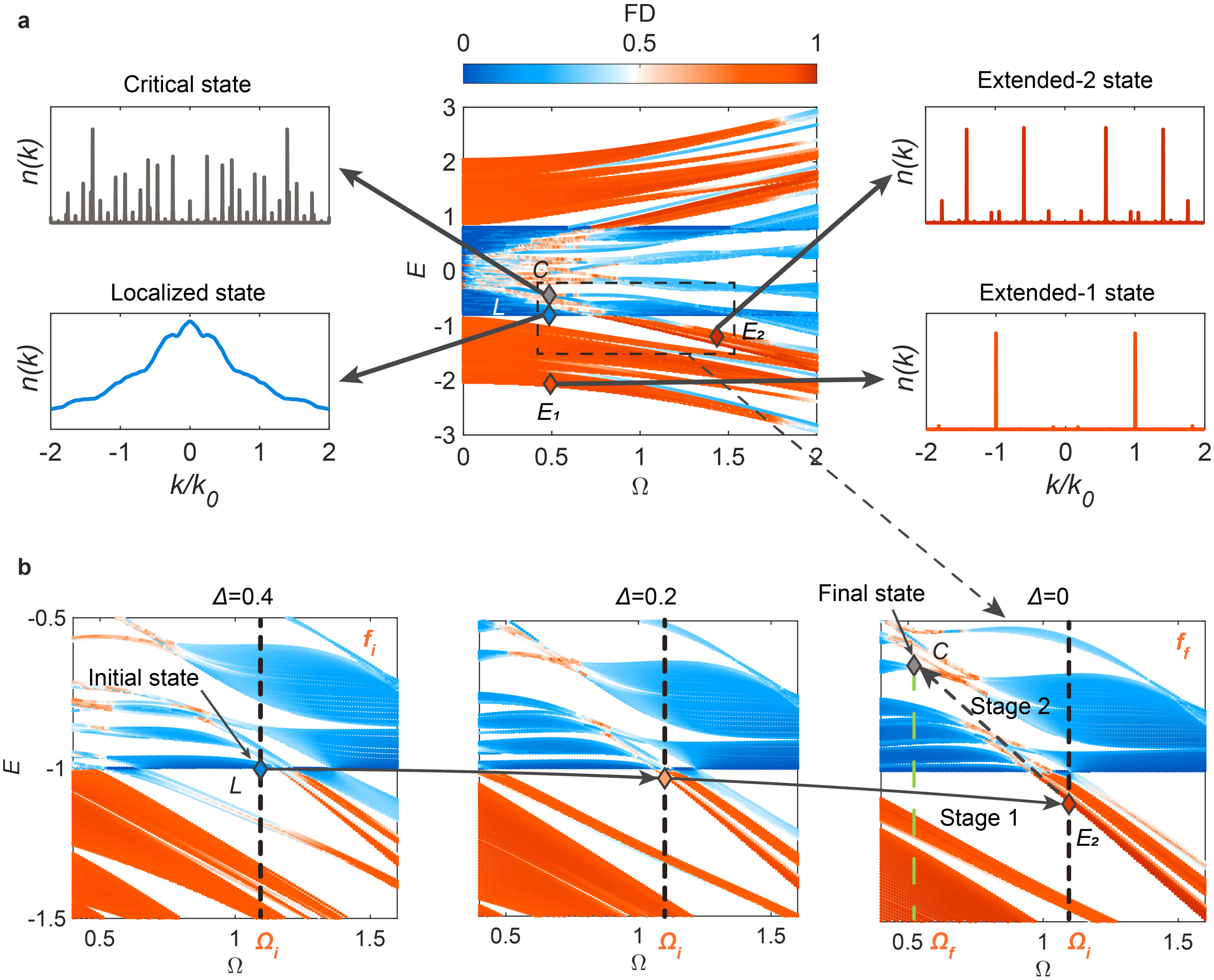

Figure S4. Schematics of the two-stage preparation protocol. **a**, Theoretical momentum distributions of typical eigenstates of Hamiltonian Eq. (8) (main text). The central panel shows the fractal dimension as a function of the coupling strength, calculated for $\Delta = 0$, $V = 1$, and $\alpha = 1.411$. The four panels on the sides display the momentum distributions corresponding to four representative states in the spectrum. **b**, Experimental schematic of the two-stage preparation protocol for generating the critical state. From left to right, the panels correspond to fractal-dimension spectra at detunings $\Delta = 0.4$, $\Delta = 0.2$, and $\Delta = 0$, which reflect the stage-1 frequency ramp from f_i to f_f. In this process, the initial localized state evolves into the E_2 state. In stage 2, a rapid ramp-down of the shaking amplitude drives the state into the critical regime by reducing the coupling strength from Ω_i to Ω_f, thereby realizing the critical state.

the frequency. In the latter case, shown in Fig. S4b, increasing the frequency from f_i to f_f shifts the E_2 branch downward in the spectrum, enabling adiabatic transfer of atoms into the E_2 state. The critical state lies in the overlap region between this extended branch and the localized s-band states. A rapid reduction of the shaking amplitude therefore drives the system nonadiabatically into this overlap regime, realizing the critical state via a Landau–Zener transition, as illustrated in Fig. S4b.

To establish a unified preparation scheme for all three types of states, we employ a two-stage protocol: in stage 1 the shaking frequency is ramped, and in stage 2 the shaking amplitude is rapidly reduced. Specifically, adiabatically ramping the frequency in stage 1 brings the s- and p-bands into resonance, transferring atoms from the localized s-band ground state into the lowest-energy p-band state (E_1). The outcome of stage 1 depends on the choice of initial frequency f_i: sweeping through the p-band minimum results in the E_1 state, while bypassing the minimum leads to the E_2 state. In stage 2, the rapid ramp-down of the amplitude leaves the E_1 state unchanged, but drives the E_2 state into the critical state.

By tuning f_i and A_i, we obtain distinct final states. For small A_i, atoms remain in the localized state. For larger A_i, the final state evolves into either an extended or a critical state depending on f_i. Specifically, with $f_i = 9\,\text{kHz}$, increasing A_i drives a transition from the localized to the extended state [Fig. S5a], whereas with $f_i = 10\,\text{kHz}$ the same variation of A_i drives the

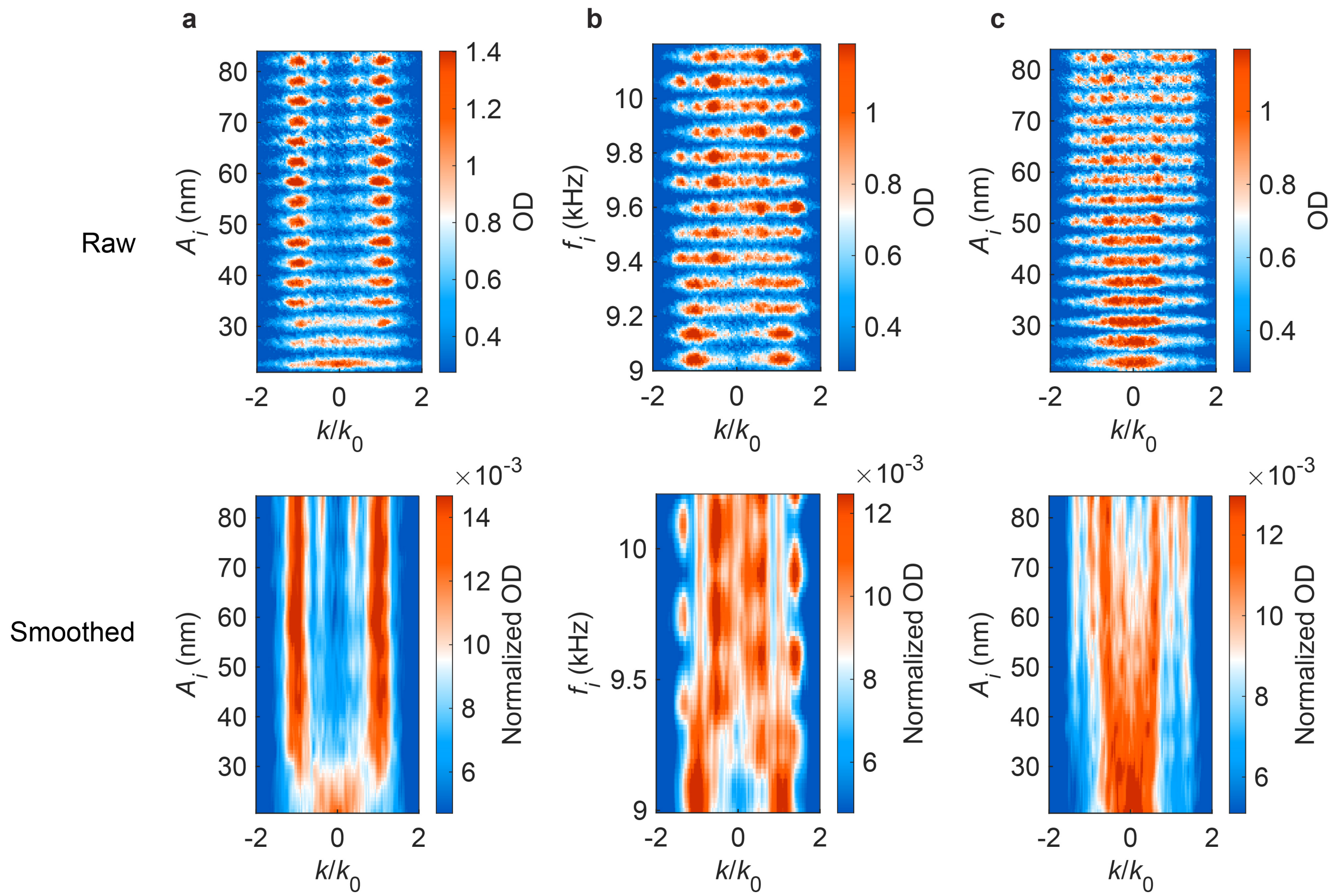

Figure S5. Different final states accessed via the two-stage protocol. **a**, For $f_i = 9\,\mathrm{kHz}$, increasing the initial shaking amplitude A_i drives the final state from localized to extended. **b**, With fixed $A_i = 63\,\mathrm{nm}$, tuning f_i drives the final state from extended to critical. **c**, For $f_i = 10\,\mathrm{kHz}$, varying A_i drives the system from localized to critical. Upper rows show raw TOF images; lower rows show the corresponding smoothed profiles used throughout the main text figures.

system from localized to critical [Fig. S5c]. Fixing $A_i = 63\,\mathrm{nm}$ and varying f_i instead takes the system from extended to critical [Fig. S5b]. These three cases correspond to the three distinct preparation paths illustrated in Fig. 3 of the main text.

Figure S5 presents both the raw TOF images (upper row) and the smoothed profiles (lower row); the latter are used in all other figures of the manuscript. The raw OD images are obtained directly from absorption imaging. For each data point, we integrate the OD along the y direction to obtain the one-dimensional momentum distribution $n(k_x)$. This distribution is then normalized within the first two Brillouin zones as

$$n_{\mathrm{norm}}(k_x) = \frac{n(k_x)}{\int \mathrm{d}k_x\, n(k_x)}. \tag{S20}$$

The normalized distributions $n_{\mathrm{norm}}(k_x)$ from different parameter points are subsequently concatenated and interpolated smoothly between parameter values, yielding the smoothed profiles shown in the lower rows.

S4. NUMERICAL SIMULATION

We present a theoretical framework to simulate the preparation of distinct quantum states by numerically solving the spatially discretized Schrödinger equation for atoms in a one-dimensional shaken optical lattice. To simplify the system, we model it in one dimension.

$$i\hbar \frac{\partial \psi(\mathbf{x},t)}{\partial t} = e^{-i\gamma}\left[-\frac{\hbar^2}{2m}\nabla^2 + V_{\mathrm{tot}}(\mathbf{x},t)\right]\psi(\mathbf{x},t), \tag{S21}$$

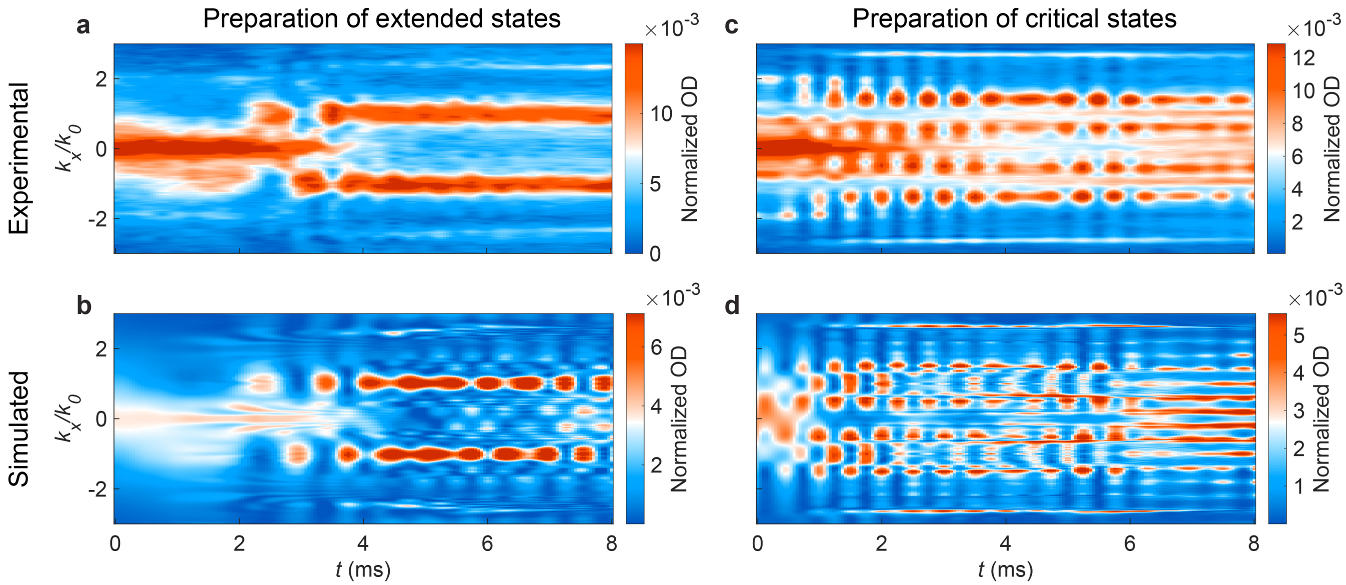

Figure S6. Experimental and simulated time slices of preparation for different states. **a,b** show the time evolution of the momentum distribution of preparation of the extended state. From 0 to 5 ms, the system is prepared from the localized state to the extended ground state E_1, then from 5 to 7 ms, the coupling strength is decreased while it remains in the extended ground state, which then also stays stable with a constant Hamiltonian for the last 1 ms holding. **c,d** show the time evolution of the momentum distribution of the critical state. From 0 to 5 ms, the system is prepared from a localized state to the E_2 state, then from 5 to 7 ms it is prepared into the critical state, which remains stable for the last 1 ms with a constant Hamiltonian. Here, **a,c** show the experimental results, while **b,d** present the simulated results, which are in good agreement. The measurements are taken with a time step of 0.25 ms for both experimental and simulated results.

where $\psi(\mathbf{x},t)$ is the condensate wavefunction, $\hbar$ the reduced Planck constant, m the atomic mass, and ∇^2 the Laplacian. Dissipation is phenomenologically incorporated via the factor $e^{-i\gamma}$[14]. The total potential $V_{\text{tot}}(\mathbf{x},t) = V_{\text{DT}}+V_{\text{p}}+V_{\text{q}}$ comprises: (i) a harmonic confinement $V_{\text{DT}} = \frac{1}{2}\omega^2x^2$; (ii) a primary lattice $V_{\text{p}}(x) = V_{\text{p}}\sin^2(k_{\text{p}}x)$ of wavelength $\lambda_{\text{p}} = 1064\,\text{nm}$; and (iii) a quasiperiodic lattice $V_{\text{q}}(x) = V_{\text{q}}\sin^2(k_{\text{q}}x)$ of wavelength $\lambda_{\text{q}} = 755\,\text{nm}$. For completeness, we set $k_\alpha = 2\pi/\lambda_\alpha$ and $E_\alpha = \hbar^2k_\alpha^2/(2m)$ for $\alpha \in \{\text{p},\text{q}\}$.

Although the Gross–Pitaevskii equation is commonly employed to model the dynamics of interacting Bose–Einstein condensates, we instead adopt the single-particle Schrödinger equation in the present study. This simplification is justified by the weak transverse confinement of the optical potential, which gives rise to a broad radial distribution and therefore a significantly reduced three-dimensional atomic density, rendering the mean-field interaction energy negligible compared with the total system energy. For our parameters, the atomic cloud prior to the shaking process exhibits a radial size of approximately 25 µm and spans roughly 30–40 lattice sites along the x direction, leading to a dilute spatial density that suppresses interaction-induced nonlinearities. The mean-field interaction energy can be estimated as $E_{\text{int}} = UN_{\text{ave}}$, where N_{ave} is the average atom number per lattice site and $U = \frac{4\pi\hbar^2 a_s}{m}\int|\psi(\mathbf{r})|^4\,d^3\mathbf{r}$. By approximating $\psi(\mathbf{r})$ with a noninteracting Gaussian wavefunction of the measured transverse width, we find that the mean-field contribution amounts to less than 1 % of the total energy. Consequently, the interaction effect remains perturbative throughout the dynamics, and the essential physics can be captured within a non-interacting single-particle framework.

The initial state at $t = 0$ is obtained by solving the stationary Schrödinger equation with parameters matched to the experiment: $\omega = 20\,\text{Hz}$, $V_{\text{p}} = 8.7E_{\text{p}}$, and $V_{\text{q}} = 1.6E_{\text{q}}$. We simulate the subsequent momentum evolution using the experimental driving sequence, represented by a time-dependent displacement of the quasiperiodic lattice. During the first 1 ms, the extended and critical protocols are initiated at driving frequencies of 8 kHz and 10 kHz, respectively, while the shaking amplitude is ramped from zero to 63 nm. From 1 ms to 5 ms, the amplitude is kept constant as the frequency is linearly increased to 10.8 kHz, steering the system along the two protocols into the intermediate E_1 and E_2 manifolds. Between 5 ms and 7 ms, the frequency remains fixed while the amplitude is reduced to 21 nm. In the final 1 ms, both the drive frequency and amplitude are held constant, rendering the Hamiltonian time-independent. The simulated momentum distributions for these preparation sequences, presented in Fig. S6, show good overall agreement with the experimental data, indicating that the main features of the observed dynamics are reproduced by the simulations.

For clarity of presentation, we select a representative set of parameters that most transparently reveals the underlying physical behavior. Although the values of V_p and the shaking frequency used in the numerical simulations differ slightly from those used in the experiment, both experimental observations and theoretical analyses demonstrate that the global phase diagram and the characteristic time-slice dynamics remain essentially unchanged over a broad parameter range. This robustness ensures that the minor parameter mismatch does not affect the physical interpretation of the results. Such discrepancies between experiment and simulation arise from slow optical-path drifts, slight miscalibrations of the lattice depth, limited accuracy of the phenomenological dissipation term, or other uncontrolled experimental factors. These effects, though unavoidable in realistic conditions, are secondary in nature and do not alter the overall agreement between theory and experiment.

S5. EXTRACTION AND ANALYSIS OF CHARACTERISTIC LENGTH SCALES

To quantitatively differentiate the localized, extended, and critical states prepared via our two-stage protocol, we employ a dual-space perspective utilizing two complementary characteristic length scales: the spatial coherence length L_{Coh} and the momentum-space correlation length k_{Cor}. Because a critical state exhibits a multifractal wave function that evades standard localization in both real and reciprocal domains, relying on a single observable is insufficient. By simultaneously mapping the behavior of both L_{Coh} and k_{Cor}, we establish a robust framework to resolve the tripartite phase diagram.

The first observable, L_{Coh}, quantifies the characteristic spatial correlations and the degree of localization within the atomic ensemble. Invoking the Wiener-Khinchin theorem, the momentum distribution $n(k)$ is fundamentally linked to the first-order spatial correlation function $G(x', x + x') = \langle \hat{\Psi}^{\dagger}(x') \hat{\Psi}(x + x') \rangle$. Specifically, the power spectrum of the field (the momentum density) is the Fourier transform of its autocorrelation, expressed through the relation [15]:

$$n(k) \propto \mathfrak{F}^{-1}\left[\int G(x', x + x') \, \mathrm{d}x'\right], \tag{S22}$$

where $\mathfrak{F}$ denotes the Fourier transform operator. In our analysis, we utilize the inverse relation to extract the spatial information from the experimental observables. We define $S(x) = \mathfrak{F}[n(k)]$, which represents the ensemble-averaged spatial correlation. The spatial coherence length is then defined as the normalized first moment of the absolute correlation function:

$$L_{\mathrm{Coh}} = \frac{\int_0^{x_{\max}} \mathrm{d}x \, |S(x)x|}{\int_0^{x_{\max}} \mathrm{d}x \, |S(x)|}. \tag{S23}$$

Physically, L_{Coh} reflects the competition between the intrinsic localization length of the wave functions and the many-body coherence of the system. In the experiment, the extracted absolute values of L_{Coh} are inherently smaller than those of an ideal pure eigenstate. This reduction is primarily driven by thermalization and decoherence effects, as the macroscopic atomic gas occupies a statistical manifold of multiple states. Nevertheless, the relative distinction between the localized and extended phases is dominantly governed by the intrinsic spatial extent of the underlying constituent wave functions. Therefore, L_{Coh} effectively captures the localization-to-delocalization transitions, enabling us to differentiate the quantum states despite the many-body dephasing.

In practice, the extraction of L_{Coh} involves a specific data processing pipeline to isolate the lattice physics from external confinement effects. First, the raw two-dimensional Time-of-Flight (TOF) images are integrated along the transverse direction to yield the 1D momentum density $n(k)$. After computing $S(x)$, we evaluate the integral over a truncated domain bounded by $x_{\max} = 5d$ (where $d = 532\,\mathrm{nm}$ is the primary lattice constant). This choice of $x_{\max}$ is crucial: it is significantly smaller than the typical characteristic length of the global harmonic confinement ($\approx 2.4\,\mu\mathrm{m}$), ensuring that the captured signal is not dominated by the external trap geometry. To further align with the discrete symmetry of the lattice, we retain only the correlation amplitudes at integer lattice sites $x_j = jd$ ($j \in \{0, 1, \ldots, 5\}$), resulting in a discrete summation for the final calculation of L_{Coh}.

Complementary to the real-space analysis, the density-density correlation length k_{Cor} is introduced to quantify the characteristic spread and fragmentation of the quantum states in reciprocal space. We first calculate the momentum-space autocorrelation function $C(k)$, defined as:

$$C(k) = \int_{-2k_0}^{2k_0} n(k' + k) n(k') \, \mathrm{d}k', \tag{S24}$$

where k_0 represents the characteristic momentum scale of the lattice. The correlation length is subsequently extracted through the normalized first moment of $C(k)$:

$$k_{\mathrm{Cor}} = \frac{\int_0^{k_0} |C(k)k| \, \mathrm{d}k}{\int_0^{k_0} |C(k)| \, \mathrm{d}k}. \tag{S25}$$

This observable provides a sensitive probe for the underlying momentum structure. An extended state, characterized by well-defined and sharp Bragg peaks, yields a highly localized autocorrelation profile $C(k)$, thereby minimizing k_{Cor}. In contrast, both localized and critical states lack long-range spatial periodicity, resulting in broad, highly fragmented momentum profiles. This reciprocal-space spreading drives a substantially larger k_{Cor}, establishing it as an essential metric for distinguishing fully extended states from the rest of the phase diagram.

By synthesizing the behaviors of L_{Coh} and k_{Cor}, we identify Region I as the localized phase (suppressed L_{Coh}, large k_{Cor}), Region II as the extended phase (large L_{Coh}, minimized k_{Cor}), and Region III as the critical phase, which features a unique "dual-delocalization" signature (simultaneously large L_{Coh} and k_{Cor}). To rigorously validate these experimental extractions, we benchmark our results against numerical simulations as detailed in the preceding section. By adopting parameters that directly match the experimental conditions, we calculate the theoretical final momentum distributions. Crucially, both the theoretical and experimental momentum density profiles are subjected to the exact same data processing pipeline—including the identical spatial truncation and discrete integration methodology—to extract the characteristic length scales. This systematic comparison demonstrates good agreement, confirming that the dual-space characteristic functions reliably map the tripartite phase diagram.

S6. MICROMOTION OF THE STATES

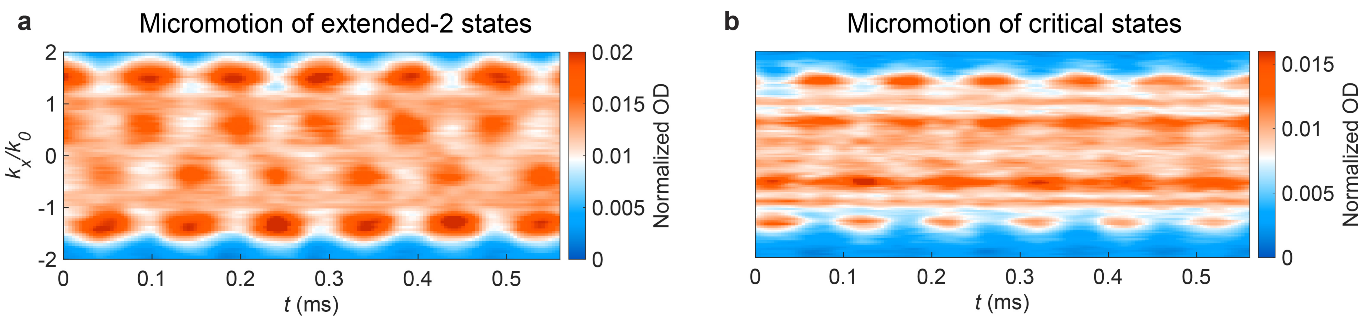

Figure S7. Experimental results for the E_2 state (**a**) and the critical state (**b**). After preparing the atoms in these states, we hold the Hamiltonian and measure the momentum distribution as a function of time. In both cases, the momentum peaks alternate between the left and right sides, oscillating at the final driving frequency $f_f = 10.2\,\mathrm{kHz}$. The measurements are taken with a time step of $0.02\,\mathrm{ms}$, and each data point represents the average of four images. For clarity, the images are further processed by smoothing.

In a Floquet-driven system, the atomic states are characterized not only by their long-term stroboscopic evolution but also by a fast periodic evolution within each driving cycle, known as micromotion [9–11, 13]. While the effective Hamiltonian $\hat{H}_{\mathrm{eff}}$ captures the time-independent physics when the system is sampled at integer multiples of the driving period $T = 1/f_f$, the true time-dependent state $|\psi(t)\rangle$ continues to evolve according to the full Hamiltonian $\hat{H}(t)$. This micromotion reflects the periodic population exchange and phase evolution between the coupled s and p bands, manifesting as high-frequency oscillations of observable quantities at the modulation frequency.

To experimentally resolve these fast dynamics, we perform TOF measurements with high temporal resolution after the adiabatic preparation sequence. Once the system reaches the target state, we hold the Hamiltonian parameters constant and record the momentum distribution at various time delays within the driving cycle. As illustrated in Fig. S7, the micromotion is clearly manifested as a periodic redistribution of the momentum density. Specifically, the momentum peaks are observed to alternate between the left and right sides of the Brillouin zone, oscillating precisely at the final driving frequency $f_f = 10.2\,\mathrm{kHz}$. This "sloshing" motion in momentum space is a direct consequence of the time-dependent interference between the s and p orbital components, which possess different spatial parities.

The experimental results for both the E_2 state (an excited extended state) and the critical state are shown in Fig. S7a and Fig. S7b, respectively. Both states exhibit pronounced micromotion, which serves as a sensitive probe of their orbital composition. The observation of these oscillations confirms that these states are not merely stationary states of the primary lattice, but are instead dynamic dressed states emerging from the strong, resonant s–p coupling induced by the shaken quasiperiodic potential. Each data point in these plots represents an average of four independent images taken with a fine time step of $0.02\,\mathrm{ms}$ (approximately $1/5$ of a driving period), ensuring that the fast oscillations are accurately captured without aliasing. The high contrast of the micromotion in the critical regime further underscores the significant role of interband hybridization in the formation of the tripartite quantum phase.

S7. EXPANSION DYNAMICS

We experimentally observe that the density distribution after a finite expansion time exhibits a bimodal profile: a fraction of atoms expands rapidly while the remainder stays localized. A likely origin is incomplete adiabatic transfer during the state-preparation sequence, leaving a portion of atoms in the initial s-band localized state rather than being excited into the p-band coupled regime. The relative fraction of atoms successfully prepared into the target state depends on the amplitude of the first shaking stage A_i, as shown in Fig. 4d of the main text.

The results obtained by varying different preparation parameters are summarized in Fig. S8. The data used for Figs. 4e,f in the main text are extracted from these measurements. As shown in Fig. S8a, increasing A_i at fixed f_i drives the final state from localized to critical. In the localized regime, atoms show negligible expansion; in the critical regime, the expansion radius grows as $t^{0.5}$. In Fig. S8b, we fix a relatively large A_i and vary f_i, driving the system from the extended to the critical regime. The dynamical exponent extracted from the time dependence changes continuously from 1 to 0.5, consistent with theoretical predictions for the three distinct transport phases [6, 16].

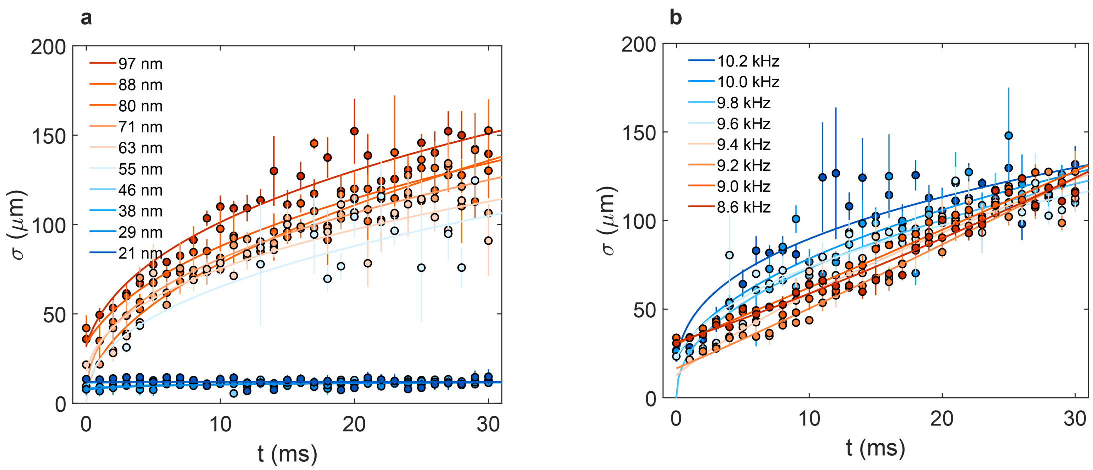

Figure S8. Expansion dynamics under different preparation parameters. **a**, Measured radius as a function of expansion time for varying A_i at fixed $f_i = 10\,\mathrm{kHz}$. For small A_i the atoms remain localized with negligible expansion, whereas larger A_i drives the system into the critical regime with diffusive spreading. **b**, Measured radius for varying f_i at fixed $A_i = 75\,\mathrm{nm}$. As f_i increases, the expansion crosses over from approximately linear to square-root scaling in time. Dots are experimental data; solid lines are power-law fits.

For the expansion measurements we use a characteristic timescale of $30\,\mathrm{ms}$, within which clear broadening of the atomic cloud is already visible. The relatively large p-band hopping amplitude ($J_p \sim 0.5\,\mathrm{kHz}$) ensures that the expansion is significant on this timescale. At longer times, drive-induced heating and decoherence thermalize the system, causing the diffusion dynamics of all states to converge, as shown in Fig. S9b.

We also monitor the total atom number throughout the evolution, as shown in Fig. S9a. All three states exhibit lifetimes exceeding $200\,\mathrm{ms}$, confirming that atom loss is negligible within the observation window.

To characterize the diffusion quantitatively, we record the in-situ normalized density distribution $n(x,t)$ after holding the Hamiltonian for time t. Density profiles are normalized such that $\int n(x,t)\,\mathrm{d}x = 1$, and pixels with optical density below zero are discarded to suppress background noise. From the double-Gaussian fits described in the Methods, we compute the second spatial moment

$$\langle x^2 \rangle = \int_{x_{\min}}^{x_{\max}} n_{\mathrm{fit}}(x,t)\,(x-\bar{x})^2\,\mathrm{d}x, \tag{S26}$$

where $\bar{x}$ is the mean position and the integration window is $\pm 200\,\mu\mathrm{m}$ around the cloud center, chosen to include the full expanding distribution.

During the first $30\,\mathrm{ms}$, the extended, critical, and localized states display clearly distinct diffusion behaviors. Beyond $30\,\mathrm{ms}$ the dynamics of all three states gradually converge, primarily due to drive-induced heating, background collisions, and partial decay of atoms back into the s-band. Accordingly, power-law fits to the expansion data are restricted to the first $30\,\mathrm{ms}$, where the measured dynamics faithfully reflect the transport properties of the prepared state.

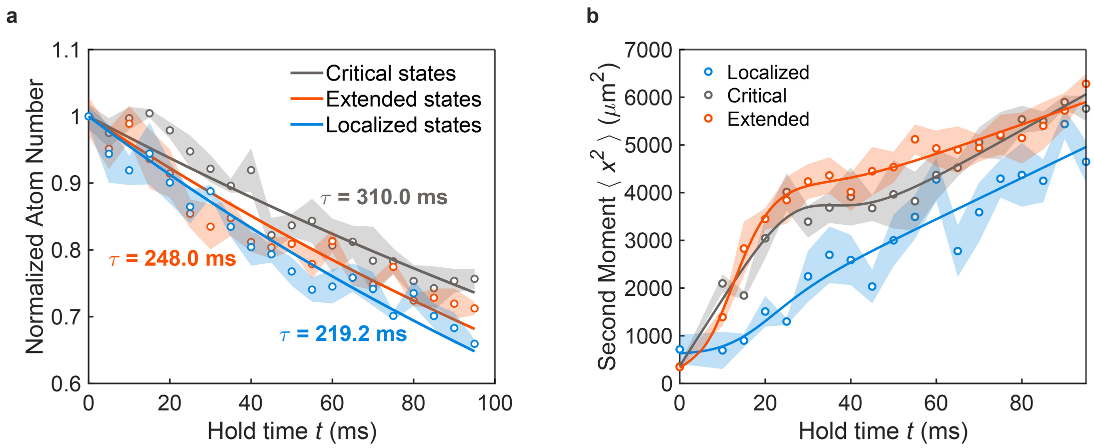

Figure S9. Long-time atom number and diffusion dynamics for atoms prepared in different final states. **a**, Normalized total atom number as a function of time for the extended, critical, and localized states, prepared with parameters $(A_i,\ f_i) = (63\,\mathrm{nm},\ 9\,\mathrm{kHz})$, $(63\,\mathrm{nm},\ 10\,\mathrm{kHz})$, and $(21\,\mathrm{nm},\ 10\,\mathrm{kHz})$, respectively. All three states retain more than $1/e$ of their initial atom number beyond $100\,\mathrm{ms}$. Solid lines are exponential decay fits. **b**, Long-time evolution of the second spatial moment $\langle x^2 \rangle$, calculated from normalized in-situ density profiles within a symmetric window of $\pm 200\,\mu\mathrm{m}$. The three states show distinct diffusion behaviors during the first $30\,\mathrm{ms}$, after which the curves converge due to classical thermalization. Solid lines are guides to the eye.

---

[1] Avila, A. Global theory of one-frequency schrödinger operators (2015).

[2] Zhou, X.-C., Wang, Y., Poon, T.-F. J., Zhou, Q. & Liu, X.-J. Exact new mobility edges between critical and localized states. *Phys. Rev. Lett.* **131**, 176401 (2023). URL `https://link.aps.org/doi/10.1103/PhysRevLett.131.176401`.

[3] Zhou, X.-C. *et al.* The fundamental localization phases in quasiperiodic systems: A unified framework and exact results. *arXiv preprint arXiv:2503.24380* (2025).

[4] Gonçalves, M., Amorim, B., Castro, E. V. & Ribeiro, P. Hidden dualities in 1D quasiperiodic lattice models. *SciPost Phys.* **13**, 046 (2022). URL `https://scipost.org/10.21468/SciPostPhys.13.3.046`.

[5] Gonçalves, M., Amorim, B., Castro, E. V. & Ribeiro, P. Renormalization group theory of one-dimensional quasiperiodic lattice models with commensurate approximants. *Phys. Rev. B* **108**, L100201 (2023). URL `https://link.aps.org/doi/10.1103/PhysRevB.108.L100201`.

[6] Wang, Y., Zhang, L., Sun, W., Poon, T.-F. J. & Liu, X.-J. Quantum phase with coexisting localized, extended, and critical zones. *Phys. Rev. B* **106**, L140203 (2022). URL `https://link.aps.org/doi/10.1103/PhysRevB.106.L140203`.

[7] Wang, Y. *et al.* One-dimensional quasiperiodic mosaic lattice with exact mobility edges. *Physical Review Letters* **125**, 196604 (2020). URL `https://link.aps.org/doi/10.1103/PhysRevLett.125.196604`.

[8] Li, X., Pixley, J. H., Deng, D.-L., Ganeshan, S. & Das Sarma, S. Quantum nonergodicity and fermion localization in a system with a single-particle mobility edge. *Phys. Rev. B* **93**, 184204 (2016). URL `https://link.aps.org/doi/10.1103/PhysRevB.93.184204`.

[9] Eckardt, A. Colloquium: Atomic quantum gases in periodically driven optical lattices. *Reviews of Modern Physics* **89**, 011004 (2017). URL `https://link.aps.org/doi/10.1103/RevModPhys.89.011004`.

[10] Bukov, M., D'Alessio, L. & Polkovnikov, A. Universal high-frequency behavior of periodically driven systems: from dynamical stabilization to floquet engineering. *Advances in Physics* **64**, 139–226 (2015). URL `https://doi.org/10.1080/00018732.2015.1055918`.

[11] Goldman, N. & Dalibard, J. Periodically driven quantum systems: Effective hamiltonians and engineered gauge fields. *Phys. Rev. X* **4**, 031027 (2014). URL `https://link.aps.org/doi/10.1103/PhysRevX.4.031027`.

[12] Song, B. *et al.* Realizing discontinuous quantum phase transitions in a strongly correlated driven optical lattice. *Nature Physics* **18**, 259–264 (2022). URL `https://doi.org/10.1038/s41567-021-01476-w`.

[13] Sun, J. *et al.* A quantitative study of the micromotion of a p-band superfluid in a shaking lattice. *Journal of Physics B: Atomic, Molecular and Optical Physics* **56**, 095302 (2023). URL `https://doi.org/10.1088/1361-6455/acc4f9`.

[14] Anderson, B. M. *et al.* Direct lattice shaking of bose condensates: Finite momentum superfluids. *Phys. Rev. Lett.* **118**, 220401 (2017). URL `https://link.aps.org/doi/10.1103/PhysRevLett.118.220401`.

[15] Deissler, B. *et al.* Delocalization of a disordered bosonic system by repulsive interactions. *Nature Physics* **6**, 354–358 (2010). URL `https://doi.org/10.1038/nphys1635`.

[16] Saha, M., Maiti, S. K. & Purkayastha, A. Anomalous transport through algebraically localized states in one dimension. *Phys. Rev. B* **100**, 174201 (2019). URL `https://link.aps.org/doi/10.1103/PhysRevB.100.174201`.